Flexible, auxetic and strain-tunable two dimensional penta-X_2C family for water splitting photocatalyst with high carrier mobility

Journal:	*Journal of Materials Chemistry A*
Manuscript ID	TA-ART-12-2018-012405.R1
Article Type:	Paper
Date Submitted by the Author:	25-Feb-2019
Complete List of Authors:	Sun, Songsong; Southwest Jiaotong University Meng, Fanchen; Clemson University, Department of Physics and Astronomy Xu, Yuanfeng; Shandong Jianzhu University He, Jian; Clemson University Ni, Yuxiang; Southwest Jiaotong University, School of Physical Science and Technology wang, hongyan; Southwest Jiaotong University, ;

Journal Name

ARTICLE TYPE

Cite this: DOI: 10.1039/xxxxxxxxxx

Flexible, auxetic and strain-tunable two dimensional penta-X_2C family for water splitting photocatalyst with high carrier mobility†

Songsong Sun,[‡a] Fanchen Meng,[‡b] Yuanfeng Xu,[c] Jian He,[b] Yuxiang Ni,[*a] and Hongyan Wang[*a]

Received Date
Accepted Date

DOI: 10.1039/xxxxxxxxxx

www.rsc.org/journalname

Two dimensional materials have been regarded as promising candidates for photocatalytic water splitting. Herein, we systematically investigated the potential of novel two dimensional penta-X_2C (X = P, As, Sb) family for photocatalytic water splitting by means of density functional theory. The penta-X_2C family are semiconductors with indirect band gaps of 2.64 eV, 2.09 eV and 1.35 eV for X = P, As and Sb, respectively. Notably, the band edges position of penta-P_2C and penta-As_2C can perfectly satisfy the redox potentials of photocatalytic water splitting via strain engineering, whereas penta-Sb_2C only meets the reduction potential. The ultrahigh (up to $10^3 \sim 10^5$ $cm^2V^{-1}s^{-1}$) and anisotropic carrier mobilities are crucial to suppressing the photogenerated electron-hole pairs recombination. Meanwhile, the penta-X_2C family exhibits excellent light absorption in visible-ultraviolet region, favorable for the utilization of sunlight. In addition, compared with other common 2D materials such as graphene and h-BN, the penta-X_2C family possesses relatively smaller Young's modulus and larger critical strain, while penta-X_2C have large negative Poisson's ratio of -0.103, -0.079 and -0.077, respectively. These results testify that the penta-X_2C family have potential applications not only in photocatalytic water splitting but also in designing 2D electromechanical and optoelectronic devices.

1 Introduction

In the wake of global energy and environmental crisis associate with the use of fossil fuels, hydrogen has been regarded as one of the most promising renewable energy resources in the future.[1–4] The combustion production of hydrogen is water only and the its energy yield per unit mass is much more than those of fossil fuels. Hence, photocatalytic water splitting has evoked much research interest as an feasible and efficient route for generating hydrogen using solar energy, which is low-cost, environmentally friendly, and renewable. Since the first discovery of photocatalytic water splitting on TiO_2 electrodes by Fujishima and Honda,[5] a wide variety of bulk semiconductor materials, including ZnO,[6] Bi_2O_3,[7] Bi_2WO_6[8] and CdS,[9] have been developed as photocatalysts for hydrogen production. However, there is still a long way to go for the industrialization of hydrogen production from photocatalytic water splitting owing to the poor light harvesting, low quantum efficiency, insufficient catalysts activity, and fast reverse reaction, *etc.*[10,11] All of these limitations in bulk semiconductors mainly derived from several of their intrinsic properties: (i) the traditional bulk semiconductors usually own wide band gaps (> 3.0 eV), which results in the absorption of the ultraviolet light only;[12,13] (ii) the recombination of photogenerated electron-hole pairs will occur easily due to the long migration distance;[14] (iii) the majority of the reaction active sites in the bulk semiconductor cannot be exposed to surface to take part in the photocatalytic reaction.[15] In this regard, two dimensional (2D) semiconductors are a materials natural solution for high efficiency photocatalytic water splitting.

Over the past decade, 2D materials are an emerging field since the discovery of mechanically exfoliated graphene in 2004[16] because of their outstanding electronic and optical properties, and potential applications in optoelectronic devices and photocatalytic water splitting. Among them, the typical representative of graphitic carbon nitrides (g-C_3N_4) has been both theoretically and experimentally identified as an potential photocat-

---

[a] *Key Laboratory of Advanced Technology of Materials (Ministry of Education), School of Physical Science and Technology, Southwest Jiaotong University, Chengdu 610031, China.*
[b] *Department of Physics and Astronomy, Clemson University, Clemson 29634, USA.*
[c] *School of Science, Shandong Jianzhu University, Jinan 250101, Shandong, China.*
Corresponding author e-mail: yuxiang.ni@swjtu.edu.cn; hongyanw@swjtu.edu.cn

† Electronic Supplementary Information (ESI) available: See DOI: 10.1039/cXCP00000x/

‡ These authors contributed equally to this work.

alyst for water splitting.[17,18] Moreover, many other 2D materials including graphene oxides,[19] transition-metal dichalcogenides (e.g. MoS_2, $MoSe_2$, WS_2),[20–22] black phosphorene,[23] transition metal carbides/nitrides (MXenes),[24] Group-III Monochalcogenide,[25] group III–VI 2D materials,[26–28] and Group-IVB nitride halides,[29], whose electronic, optical, and catalysis properties are markedly different from their bulk materials, have been proven to be suitable photocatalysts. The 2D materials possess unique inherent superiority to improve the efficiency of photocatalytic water splitting: (i) the large surface area can provide much more adsorption sites for OH^-, H^+ and H_2O participating in the photocatalytic reaction; (ii) the relatively short carrier transport distance in 2D materials improves electron-hole migration and separation, and reduces the recombination rate; (iii) the band gaps and light harvesting of 2D materials can be modulated by mechanical strain, electrical bias, doping, and chemical bias.[10]

Numerous 2D materials such as MoS_2, g-C_3N_4, α-phosphorene and MPS_3 (M = Ni, Mn, and Fe), have been theoretically or experimentally examined to be promising as the efficient photocatalyst for water splitting to generate hydrogen in the future.[17,30–35] Nonetheless, there still exist some inherent drawbacks. For example, MoS_2 monolayer exhibit sizable bandgap of 1.8 eV, but the relatively low carrier mobility $\sim$ 200 $cm^2 \cdot V^{-1} \cdot s^{-1}$ at room temperature limits their practical application. Both g-C_3N_4 and 2D MPS_3 (M = Ni, Mn, and Fe) possess large overpotential of water oxidation half reaction, despite relatively good photocatalytic performance for water splitting to produce H_2. In addition, the monolayer germanium monochalcogenides was predicted as UV-light-driven photocatalyst because of the large band gap.[36] Therefore, there is plenty of room for the theoretical exploration of novel and applicable 2D materials for photocatalytic water splitting.

Recently, a novel 2D structure named as penta-graphene has been proposed. It consists of pentagonal rings of carbon atoms and has an intrinsic quasi-direct band gap (3.25 eV), a negative Poisson's ratio and much better ideal strength than graphene.[37] The emergence of penta-graphene has promoted various explorations for new pentagonal 2D materials, such as penta-SiC_2,[38,39] penta-Ge_2P,[40] penta-TMBs,[41] penta-Pt_2N_4,[42] *etc*. Lately, novel pentagonal 2D materials penta-P_2C, penta-As_2C, and penta-Sb_2C, have been theoretically predicted. They possess suitable and tunable band gaps of 2.76 eV, 2.22 eV, and 1.45eV, respectively, and are thermodynamically, dynamically, and thermally stable.[43–45] Unfortunately, little is known regarding the potential of the penta-X_2C family for photocatalytic water splitting. To fill this knowledge gap, in this study, we systematically investigate the structural stability, mechanical, electronic, photocatalytic and optical properties of penta-X_2C family based on density functional theory (DFT). Remarkably, according to our calculations, the penta-X_2C family has suitable indirect band gap of 2.64 eV, 2.09 eV and 1.35 eV, respectively. In addition, the penta-X_2C family presents suitable band edge alignments, which can provide adequate driving force for water splitting. As the penta-X_2C family also exhibits pronounced optical absorption in visible-ultraviolet spectrum, and possesses anisotropic and ultrahigh carrier mobility up to $10^3 \sim 10^5 cm^2 \cdot V^{-1} \cdot s^{-1}$, which are beneficial to utilizing solar energy and reducing the recombination rate of photogenerated electron-hole pairs. Besides, the mechanical properties of penta-X_2C family are interesting in their own right, *e.g.* relatively smaller Young's modulus, lager critical strain, and negative Poisson's ratio. The results indicate that the flexible and auxetic penta-X_2C family are promising 2D materials for photocatalytic water splitting hydrogen generation.

2 Computational methods

Our first-principles calculations are performed using DFT as implemented in Vienna *ab initio* simulation package (VASP).[46,47] The projected augmented wave (PAW) approach is employed to manipulate the electron and core interactions,[48] and the exchange-correlation potential is in the form of Perdew-Burke-Ernzerhof (PBE) within the generalized gradient approximation (GGA).[49] The kinetic energy cutoff for the plane-wave expansion is set to 550 eV for all calculations. Both the geometries and atomic positions are fully relaxed until the energy and Hellmann-Feynman force acting on each atom are less than 10^{-6} eV and 10^{-3} eV/Å, respectively. The irreducible Brillouin zone is represented by $11\times11\times1$ *k*-meshes within the Monkhorst-Pack scheme for the geometry relaxation and by $17\times17\times1$ *k*-meshes for the electronic structure calculations.[50] To avoid the interaction between neighbour layers, a vacuum layer of 20 Å is applied in the *z* direction. Owing to the underestimate bandgap the Heyd-Scuseria-Ernzerhof hybrid functional (HSE06) is used to correct the underestimated band gaps of semiconductors in PBE functional.[51,52]

3 Results and discussion

3.1 Crystal structures and mechanical properties of Penta-X_2C (X=P, As, Sb) monolayers

The atomic configuration of penta-X_2C (X = P, As, Sb) is shown in Fig. 1, which belongs to space group $P\text{-}42_1m$ (no.113). These pentagonal structures can be obtained via replacing four sp^3-hybridized carbon atoms in the penta-graphene unit cell with X atoms. For penta-X_2C system, each carbon atom binds to four neighboring X atoms in the square planar crystal field, while each X atom is shared by two carbon atoms and one X atom. The equilibrium lattice parameters of penta-X_2C (X = P, As, Sb) are fully optimized at PBE level as shown in Table. 1, which are in good agreement with several recent investigations.[43–45]

The thermodynamic, dynamical, and thermal stabilities of penta-X_2C (X=P, As, Sb) have been illustrated from the cohesive energy, phonon dispersion and molecular dynamic calculations.[43–45] Building upon these results, we further examine their mechanical stability and properties by calculating the change of energy respect to the in-plane strain. For a 2D material, using the standard Voigt notation,[37] i.e., 1-xx, 2-yy and 6-xy, the strain energy $U(\varepsilon)$ per unit area is expressed as[53,54]

$$U(\varepsilon)=\frac{1}{2}C_{11}\varepsilon_{xx}^2+\frac{1}{2}C_{22}\varepsilon_{yy}^2+C_{12}\varepsilon_{xx}\varepsilon_{yy}+2C_{66}\varepsilon_{xy}^2, \tag{1}$$

where the coefficients C_{ij}(i, j = 1, 2, 6) are the components of the in-plane stiffness tensor, corresponding to the second partial derivative of strain energy with respect to strain (C_{ij} =

Table 1 The calculated lattice parameters (lattice constant *a*, *b*, bond length for *X-C*, angle of *2-1-3*, *1-2-9*) band gaps E_g^{PBE} based on PBE, band gaps E_g^{HSE06} based on HSE06 for Penta-X_2C (X = P, As, Sb), respectively. Data in the parentheses are taken from Ref. 36, Ref.37 and Ref.38.

Unitcell type	a = b(Å)	Δ_{X-C}(Å)	$\angle_{2-1-3}$	$\angle_{1-2-9}$	E_g^{PBE}(eV)	E_g^{HSE06}(eV)
Penta-P_2C	4.09 (4.10)	1.88	112.37°(112°)	100.76° (101°)	1.78 (1.90)	2.64 (2.76)
Penta-As_2C	4.36(4.42)	2.02	113.41°(112.5°)	99.89° (99.98°)	1.41 (1.62)	2.09 (2.22)
Penta-Sb_2C	4.79 (4.83)	2.21	113.95 °	99.85°(100.278°)	0.80 (0.90)	1.35 (1.45)

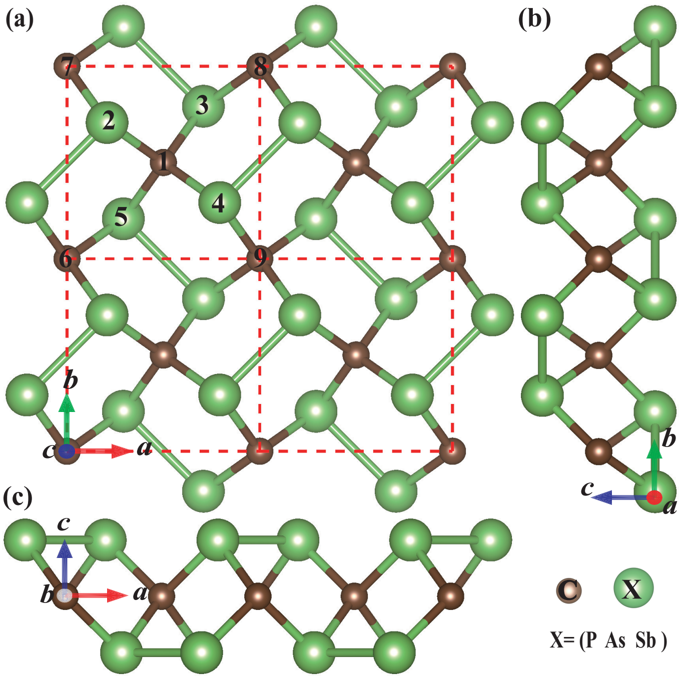

Fig. 1 (a)Top and (b) (c) side views of optimized 2×2 supercells of Penta-X_2C (X = P, As, Sb). Brown and green balls represent C and X (P, As, Sb) atoms , respectively.

$(1/S_0)(\partial^2 U(\varepsilon)/\partial\varepsilon_i\partial\varepsilon_j)$, S_0 is the area of the equilibrium unitcell). To guarantee the mechanical stability of 2D materials, the elastic constants need to satisfy the conditions of $C_{11}C_{22} - C_{12}^2 > 0$ and $C_{66} > 0$.[37] For the tetragonal symmetry of penta-X_2C (X=P, As, Sb), the necessary conditions for the mechanical stability is reduced to $C_{11} > |C_{12}|$ and $C_{66} > 0$ as a result of $C_{11} = C_{22}$. Through parabolic fitting of the strain energy under uniaxial, shear and biaxial in-plane strain, the in-plane stiffness constant C_{11}, C_{12} and C_{66} of the penta-X_2C family can be respectively derived (See Fig.S1 of ESI†). All the mechanical parameters listed in Table. 2 indicate that the penta-X_2C family monolayer are mechanically stable. Meanwhile, the mechanical properties of orientation-dependent Young's Modulus Y and Poisson's ratio ν of penta-X_2C family monolayer are explored with the expressions of Eq.S1 and Eq.S2 (ESI†), respectively. As shown in Fig. 2, the mechanical properties of penta-X_2C family are highly anisotropic. The maximum Young's modulus occurs along the diagonal direction, and Y follows the order of penta-Sb_2C < penta-As_2C < penta-P_2C because of a smaller lattice constant corresponds to a shorter bond length and stronger interaction. Meanwhile, the relatively smaller Young's modulus of penta-X_2C compared with that of graphene (340 N/m),[55] MoS_2 (180 ± 60 N/m),[56] and h-BN (292.1 N/m)[57] indicates that penta-X_2C family monolayers are more stretchable and flexible, which are important in the application of electronic devices. It's somewhat a surprise that the maximum negative Poisson's ratio (NPR) appears along the diagonal direction for penta-P_2C (-0.103), penta-As_2C (-0.079) and penta-Sb_2C (-0.077), respectively. To confirm this unusual result, a supercell was intercepted to investigate the transverse response of penta-X_2C family under a series of uniaxial tensile strains in-plane, as shown in Fig.S2 (ESI†). As expect, a small expansion is observed along the ***b*** direction, when the uniaxial tensile is along the ***a*** direction and vice versa. Meanwhile, the atomic displacement under ***a*** direction tensile strain relative to the equilibrium structure is depicted in Fig.S3 (ESI†) to unveil the underlying mechanism of negative Poisson's ration of the penta-X_2C family. When the lattice of ***a*** is uniaxially elongated, the structure of penta-X_2C family will be compressed in the ***z*** direction meaning that X atoms will move inward along the direction of the attached arrows in Fig. S3 (ESI†). The inward movement of X atoms will increase the bond angles such as θ_{157},θ_{260} θ_{780}, and $\theta_{13,14,15}$, because the bond lengths are essentially unchanged due to the strong inter-atomic forces. The natural tendency of compression in the transverse direction will be compensated and surpassed by this mechanism. Thus, the entire penta-X_2C family belongs to the so-called auxetic materials, in which the lattice of transverse direction will expand rather than compress with a uniaxial tensile strain. Note that the NPR values of penta-X_2C family are comparable or even larger than the reported values of SnSe (-0.17),[58] penta-graphene (-0.07),[37] borophene (-0.04),[59] black phosphorene (-0.03),[60] and penta-B_2N_4 (-0.02)[61] making them not only photocatalystically interesting but also mechanically appealing.

In addition, the ideal tensile strength of the penta-X_2C family is investigated by calculating the variation of stress respect to the uniaxial and biaxial tensile strains. From Fig. 3, it can be clearly seen that the ideal tensile strength of penta-P_2C, penta-As_2C and penta-Sb_2C are 14.92, 11.79 and 9.39 GPa·nm corresponding to the critical strains of 24%, 27% and 30% upon uniaxial strain, respectively. For biaxial strain, the ideal tensile strength are 19.44, 14.33 and 10.41 GPa·nm with respect to the same critical strain of 18%. The relatively smaller Young's modulus, lager critical strain, and negative Poisson's ratio endow the penta-X_2C family with significant potential applications in flexible nanomechanics, microelectronic and optoelectronic devices.

Table 2 Calculated In-plane Stiffness Constants C_{ij}, Young's Modulus Y, and Poisson's ratio v of Penta-X_2C (X = P, As, Sb), respectively.

Unitcell type	$C_{11} = C_{22}$	C_{12}	C_{66}	Y	v
Penta-P_2C	84.11	44.72	79.18	60.33	0.53
Penta-As_2C	63.77	41.07	61.46	37.32	0.64
Penta-Sb_2C	40.78	36.20	44.94	8.65	0.89

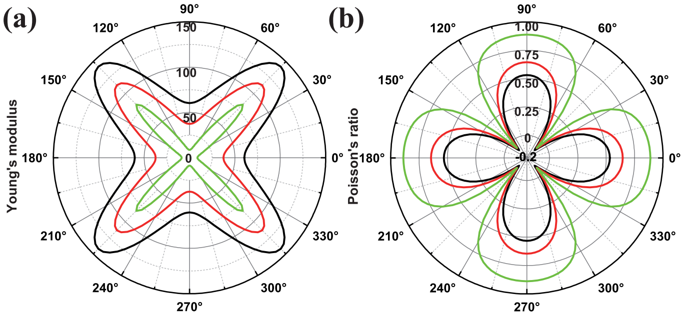

Fig. 2 Polar diagram for (a) Young's modulus and (b) Poisson's ratio of Penta-X_2C (X = P, As, Sb). θ is the angle respect to ***a*** direction. The black, red and green solid line are corresponding to Penta-P_2C, Penta-As_2C, and Pena-Sb_2C, respectively.

3.2 Electronic and photocatalytic properties of penta-X_2C (X = P, As, Sb) for water splitting

To probe the electronic properties of penta-X_2C (X = P, As, Sb) monolayer, the band structures are systematically calculated as presented in Fig. 4. Obviously, the penta-X_2C family are indirect semiconductors, with the valance band maximum (VBM) located on the Γ - ***Y*** path whereas the conduction band minimum (CBM) lies on the ***S*** - Γ path. Compared with the PBE functional, the HSE06 functional has a rigid effect on the band structure, which only corrects the band energy without changing the dispersion near the band edges. Thus, the band gaps of the penta-X_2C family are corrected to 2.64 eV, 2.09 eV and 1.35 eV, which are consistent with the results of previous studies as listed in the Table. 1. Analysis of the orbital-projected band structures as shown in Fig.S4 (ESI†) reveals that the VBM of penta-X_2C (X = P, As, Sb) family monolayers are mainly dominated by the hybridization of ***p*** orbital of X and ***p*** orbital of carbon, while the CBM are predominantly contributed by ***p*** orbital of X and partially contributed by ***s*** orbital of X. The sizable and tunable band gaps qualify penta-X_2C family as excellent candidate materials for photocatalyst and nanoelectronics.

To be an efficient photocatalyst for water splitting, several conditions need to be satisfied. Firstly, the bandgap must exceed the requirement of the oxidation reduction potential (ORP) of water splitting of 1.23 eV. Furthermore, its band edges must cross the redox potentials of water: that is, the location of the CBM should be higher than the reduction potential of H^+/H_2 (E^{H^+/H_2} =-4.44 eV, 0 V vs NHE at pH = 0) and the location of the VBM must be lower than the oxidation potential of O_2/H_2O (E^{O_2/H_2O}=-5.67 eV, 1.23 V vs NHE at pH = 0). The schematic diagram of band edges with respect to the vacuum level of penta-X_2C (X=P, As, Sb) monolayers for photocatalytic water splitting is presented in Fig. 5(a). For penta-As_2C and Sb_2C, the band edges of VBM (E_{VBM} = -5.46 eV and -4.70 eV) and CBM (E_{CBM} = -3.37 eV and -3.34 eV) are higher than the oxidation potential of O_2/H_2O and the reduction potential of H^+/H_2, respectively, while the band edges (E_{VBM} = -6.09 eV and E_{CBM} = -3.45 eV) of penta-P_2C monolayer straddle the redox potentials of water splitting at pH = 0. The energy difference between the oxidation potential (hydrogen reduction potential) and the E_{VBM} (E_{CBM}) is known as the oxidizing power (reducing power) which is found to be 0.42 eV (0.99 eV) for penta-P_2C monolayer. The values of reducing and oxidizing power indicate that only the penta-P_2C monolayer is a promising candidate for water splitting photocatalysts without an external bias voltage. For penta-As_2C and penta-Sb_2C, only the band edges of CBM are higher than the reduction potential of H^+/H_2, suggesting that they cannot product O_2 by water splitting, but they can be used to generate hydrogen on account of the large enough reducing power (1.07 eV and 1.10 eV).

However, the redox potentials are related to the pH value of the water splitting reaction, which shifts upward 59 meV as each unit of pH value increases.[10,62] The standard reduction potential for H^+/H_2 was estimated by E^{H^+/H_2}= -4.44 eV + pH×0.059 eV, while the oxidation potential for O_2/H_2O was calculated by E^{O_2/H_2O}= -5.67 eV + pH×0.059 eV. Therefore, the redox potential for water splitting reaction at pH = 7 was also calculated and marked in Fig. 5(a) ($E^{H^+/H_2}_{pH=7}$ = -4.027 eV and $E^{O_2/H_2O}_{pH=7}$ = -5.257 eV). It is obvious that apart from penta-P_2C, the band edge positions of penta-As_2C also perfectly encompass the redox potential for water splitting reaction at pH = 7, while the band edge of CBM is only higher than the reduction potential for the penta-Sb_2C monolayer. Obviously, penta-P_2C and penta-As_2C are the applicable water splitting photocatalysts at neutral environment.

Besides a proper band alignment, the efficiency of photocatalytic water splitting is also dependent on the absorption capability of the visible-ultraviolet region as it accounts for more than 45% of the solar energy. To investigate the optical absorption, the imaginary part of frequency dependent dielectric function ε_2 is calculated using the following expression:[63]

$$\varepsilon_{\alpha\beta}(\omega) = \frac{4\pi^2 e^2}{\Omega} \lim_{q\to 0} \frac{1}{q^2} \sum_{c,v,k} 2\omega_k \delta(\varepsilon_{ck} - \varepsilon_{vk} - \omega) \times \langle \mu_{ck+e_\alpha} | \mu_{vk} \rangle \langle \mu_{ck+e_\alpha} | \mu_{vk} \rangle^* \tag{2}$$

where Ω represents the volume of the unitcell, the vector e_α is the unit vector for the three Cartesian directions. The indices c and v refer to the conduction and valence band states, respectively. u_k is an eigenstate with wave vector k, and ω_k are the k-point weights. The absorption coefficient $\alpha(\omega)$ is performed by[64]

$$\alpha(\omega) = \sqrt{2}\omega\{\sqrt{\varepsilon_1^2(\omega) + \varepsilon_{\alpha\beta}^2(\omega)} - \varepsilon_1(\omega)\}^{1/2} \tag{3}$$

where ε_1 the real part of the frequency dependent dielectric function, which can be obtained using the Kramers-Kronig transformation. As shown in Fig. 5(b), we find that all of the penta-X_2C (X=P, As, Sb) monolayers exhibit obvious optical absorption within visible-ultraviolet light region, and the absorption intensity reaches the order of 10^5 cm^{-1}. Although penta-Sb_2C cannot generate O_2 by water splitting, it possesses the strongest optical

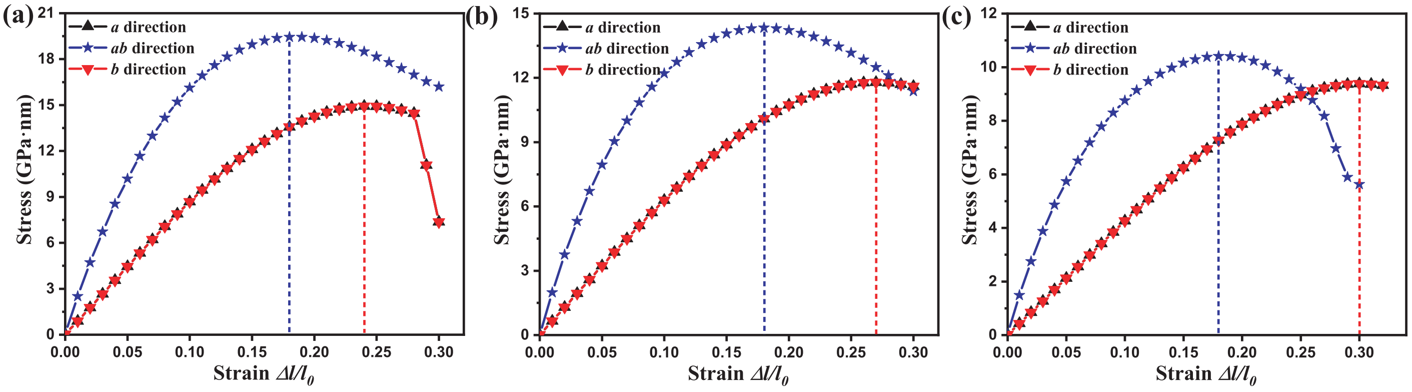

Fig. 3 The strain–stress relation of (a) Penta-P_2C (b) Penta-As_2C (c) Penta-Sb_2C with applying the uniaxial (***a*** and ***b*** direction) and biaxial (***ab*** direction) in-plane strain, respectively.

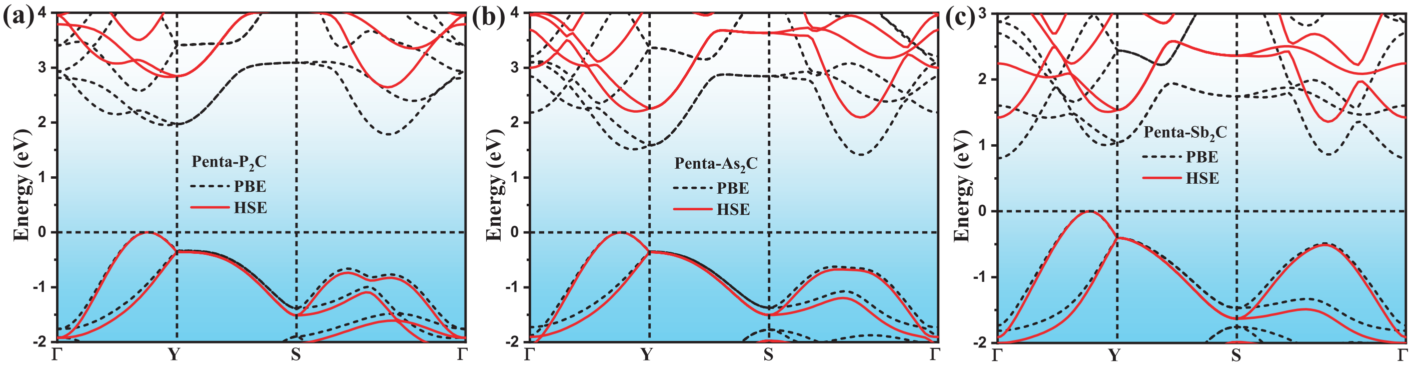

Fig. 4 Electronic band structures of (a) Penta-P_2C (b) Penta-As_2C (c) Penta-Sb_2C at the PBE (black dashed line) and HSE06 (red dashed line) level, respectively. The top of the valence band is set at zero.

absorption in the visible-ultraviolet spectrum. As for penta- P_2C and penta-As_2C, high efficiency in the utilization of solar energy can be guaranteed for photocatalytic water splitting.

3.3 Band gap and band edges position of penta-X_2C (X = P, As, Sb) tuning via strain engineering

It is known that applying external strain is a feasible technique for modulate band edge positions.[65] To better understand the electronic property-strain relationship of penta-X_2C monolayers, we investigated the band edge positions corresponding to the applied in-plane biaxial strain on the unitcell. The strain is defined as $\varepsilon = (l - l_0)/l_0$, where l and l_0 correspond to the strained and the equilibrium lattice constants, respectively. As expected, the in-plane biaxial strain has a significant effect on the band edges position of penta-X_2C family, as shown in Fig. 6. For penta-P_2C and penta-As_2C, the positions of VBM and CBM are largely shifted downward and upward respectively until the increasing tensile strain reaches to 6%, which leads to the increase of band gap to 3.15 eV and 2.55 eV. The CBM positions of penta-Sb_2C are shifted downward more intensely than the positions of VBM with the increasing tensile strain, resulting in the decrease of bandgap. The band edges position of the strained penta-P_2C monolayer well satisfy the reduction and oxidation potential of water splitting at pH = 0 and pH = 7, while the band edges position of strained penta-As_2C monolayer only satisfy the reduction and oxidation potential of water splitting at pH = 7. However, the VBM position of penta-As_2C becomes lower than the oxidation potential of O_2/H_2O (E^{O_2/H_2O}=-5.67 eV) under 6% tensile strain, which implies that it can meet the thermodynamic requirements for overall water splitting at pH = 0. For penta-Sb_2C, the band positions of VBM still cannot satisfy the oxidation potential of O_2/H_2O, and merely serves as a potential photocatalyst to generate hydrogen. The above results indicate that the band gap and band edge positions of the penta-P_2C and penta-As_2C monolayer can be flexibly modulated by applying an external strain, which could facilitate its utilization in photocatalytic water splitting.

3.4 Small effective mass and ultrahigh carrier mobility of penta-X_2C (X = P, As, Sb)

To further explore the performance of penta-X_2C family monolayers as photocatalysts for water splitting, the carrier effective mass and mobility were investigated to quantitatively describe the transfer capability of electron-hole along special directions. Based on fitting parabolic functions of the VBM and CBM locations, the carrier effective mass (m_e^* and m_h^*) of penta-X_2C family can be obtained from the following equation:

$$\frac{1}{m^*} = \frac{1}{\hbar^2}\frac{\partial^2 E(k)}{\partial k^2}, \tag{4}$$

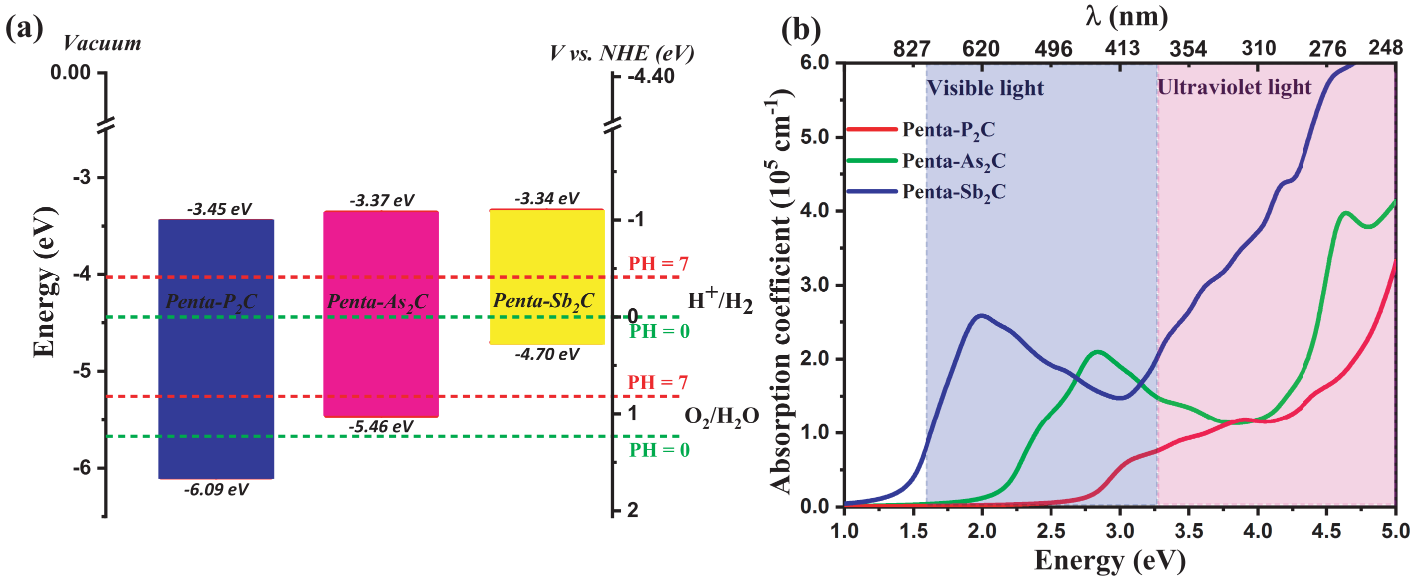

Fig. 5 (a)The location of VBM and CBM calculated with HSE06 functional of Penta-X$_2$C (X = P, As, Sb). The redox potentials of water splitting are marked by the dashed lines at pH = 0 (green) and pH = 7 (red) as shown for comparison. All the energy levels are referenced to the vacuum level, which is set to zero. (b) Optical absorption coefficient for Penta-X$_2$C (X = P, As, Sb), respectively.

where $E(k)$ is the carrier energy corresponding to the wave vector k. The carrier effective mass of penta-X$_2$C (X=P, As, Sb) are presented in Fig. 7 with all the spatial directions. It is obvious that the effective mass of hole (m_h^*) along the ***a*** direction is about twice larger than that along the ***b*** direction, while the effective masses of electron (m_e^*) are almost the same either in the ***a*** or ***b*** direction, and the m_e^* and m_h^* of penta-X$_2$C are highly anisotropic with an "8" shape on account of the dispersive ***p*** atomic orbital of X atoms mainly contributing to the VBM/CBM as shown in Fig.S5 (ESI†). According to the values of carrier effective masses as shown in Table. 3, it is predicted that the effective masses of penta-X$_2$C (X=P, As, Sb) are in general smaller than most other 2D photocatalytic materials such as Hittorf's phosphorus, (m_e/m_0 = 0.69, m_h/m_0 = 1.24) α-phosphorene (m_e/m_0 = 1.13, m_h/m_0 = 1.81), MnPSe$_3$ (m_e/m_0 = 0.55, m_h/m_0 = 1.22), SnP$_3$ (m_e/m_0 = 0.90, m_h/m_0 = 0.72) and KTlO (m_e/m_0 = 0.74, m_h/m_0 = 2.40).[32,66–69] In photocatalytic process, the transfer of photo-generate holes and electrons to the reactive sites is much easier with smaller effective masses, and the difference between effective mass of electrons and holes is larger than ~0.1 m_0, favoring to effective separation of photo-generate electron–hole pairs and the small probability of recombination for photogenerated carriers.

Furthermore, on the basis of deformation potential (DP) theory,[70] which is regulated by acoustic phonon scattering via intra- and inter-valley coupling, the carrier mobility of 2D materials can be evaluated by the following expression:[68,71]

$$\mu_{2D} = \frac{e\hbar^3 C_{2D}}{k_B T m_e^* m_d E_d^2}. \tag{5}$$

Here, $\hbar$ is the reduced Plank constant, k_B is Boltzmann constant, and T represents the temperature (300K). m_e^* is the effective mass of electron or hole along the transport direction; m_d is the carrier average effective mass which can be obtained by $m_d = \sqrt{m_a m_b}$. C_{2D} represents the in-plane stiffness determined by $C_{2D} = [\partial^2 E/\partial \delta^2]/S_0$, where E is the total energy of the supercell after deformation, and δ is the isotropic strain. The DP constant E_d, defined as $E_d = \partial E_{edge}/\partial \delta$, denotes the shift of the band edge position with respect to the isotropic strain (the step is set as 0.1%). The obtained total energy and the band edges positions with respect to the vacuum level of penta-X$_2$C (X=P, As, Sb) monolayers as a function of the isotropic strain δ along the ***a*** and ***b*** direction are illustrated in Fig.S6 and Fig.S7 (ESI†). It can be seen that the linear fittings of the band edge positions and the parabolic fitting of total energies fit well with theoretical calculations. As shown in Table. 3, the DP constants are not equal for holes along different directions, while almost the same for electrons. It is well known that the DP constant is a feature of the coupling strength of the hole or electron to the acoustic phonon.[72,73] Therefore, the scattering of holes by acoustic phonon along ***a*** direction are weaker than that of holes along ***b*** direction, while the electrons scattered by acoustic phonon is equal in the ***a*** and ***b*** directions. Since the DP constant takes a quadratic term in the denominator of Eq. 5, it has a stronger effect than other terms on the carrier mobility. For penta-P$_2$C, -As$_2$C and -Sb$_2$C, the obtained electron mobility along the ***a*** direction are $9.12 \times 10^3 cm^2V^{-1}s^{-1}$, $1.47 \times 10^3 cm^2V^{-1}s^{-1}$ and $1.94 \times 10^3 cm^2V^{-1}s^{-1}$, whereas the hole mobility along the ***a*** direction is about $1.45 \times 10^3 cm^2V^{-1}s^{-1}$, $1.52 \times 10^5 cm^2V^{-1}s^{-1}$ and $7.52 \times 10^3 cm^2V^{-1}s^{-1}$, respectively. Simultaneously, the electron mobility along the ***b*** direction is about $9.54 \times 10^3 cm^2V^{-1}s^{-1}$, $1.47 \times 10^3 cm^2V^{-1}s^{-1}$ and $1.95 \times 10^3 cm^2V^{-1}s^{-1}$, while the hole mobility along the ***b*** direction is about $0.31 \times 10^3 cm^2V^{-1}s^{-1}$, $1.05 \times 10^3 cm^2V^{-1}s^{-1}$ and $3.63 \times 10^3 cm^2V^{-1}s^{-1}$, respectively. Interestingly, although the penta-As$_2$C and penta-Sb$_2$C have smaller in-plane stiffness and larger effective mass compared with penta-P$_2$C, the hole mobility along ***a*** direction of them can reach 1.52*10^5 cm^2/V^{-1}s^{-1} and

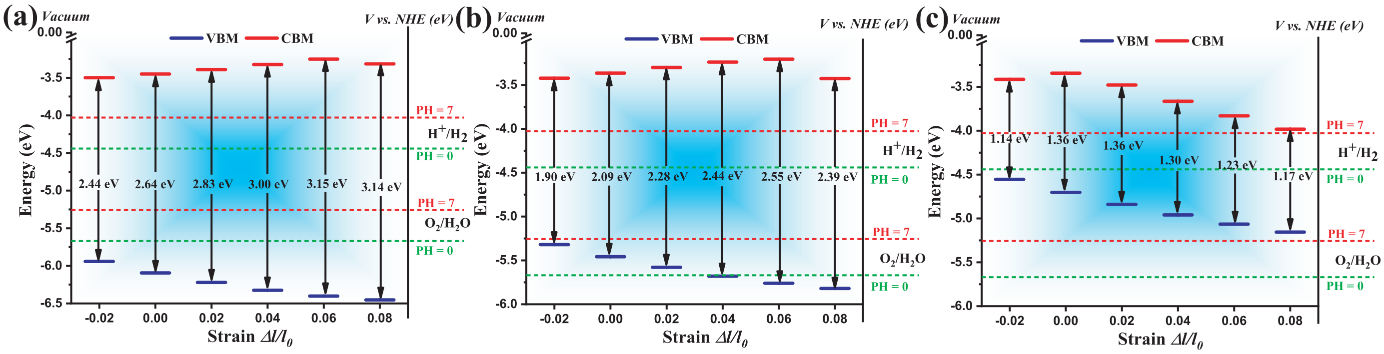

Fig. 6 Strain effects on band edge positions of (a) Penta-P_2C (b) Penta-As_2C (c) Penta-Sb_2C with respect to the vacuum level, respectively. The redox potentials (green and red dashed line for pH = 0 and pH = 7) of water splitting are shown for comparison.

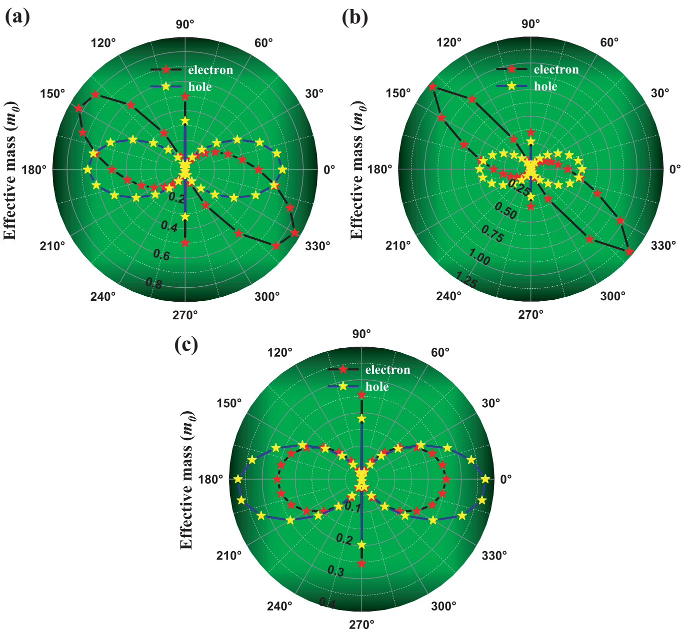

Fig. 7 Effective mass of electrons and holes for (a) Penta-P_2C (b) Penta-As_2C (c) Penta-Sb_2C according to spatial directions, respectively.

$7.52*10^3$ $cm^2/V^{-1}s^{-1}$, respectively, which is much larger than that along ***b*** direction of penta-P_2C ($0.31*10^3$ $cm^2/V^{-1}s^{-1}$). The phenomenon is attributed to the critical value of DP constants. As mentioned above, the DP constants are related to electron-acoustic-phonon interaction. Herein, for holes, the stronger electron-acoustic-phonon interaction of penta-P_2C along ***b*** direction leads to a much larger DP constant than those of penta-As_2C and penta-Sb_2C along ***a*** direction. More importantly, the carrier mobility of penta-X_2C family monolayer could be comparable with or even higher than that of many other 2D semiconductors, including $MnPSe_3$ (~626 $cm^2V^{-1}s^{-1}$), MoS_2 (~200 $cm^2V^{-1}s^{-1}$), BN (~487 $cm^2V^{-1}s^{-1}$), $PdSe_2$ (~534 $cm^2V^{-1}s^{-1}$), SiAs (~470 $cm^2V^{-1}s^{-1}$), PdPS (~312 $cm^2V^{-1}s^{-1}$) and PdPSe (~197 $cm^2V^{-1}s^{-1}$).[32,74–78] Therefore, the larger anisotropic and ultrahigh carrier mobility can dramatically reduce the recombination rate of photo-generated electrons and holes, instead, they can fast migrate to the surface of the penta-X_2C (X = P, As, Sb) to take part in the redox reaction of water splitting, which is favorable for the long-term photocatalytic activity.

4 Conclusions

In conclusion, our theoretical work show that the penta-X_2C family are all semiconductors with suitable indirect band gaps of 2.64 eV, 2.09 eV and 1.35 eV, respectively. Attractively, penta-P_2C and penta-As_2C present appropriate band edge positions straddling the water redox potentials via strain engineering, whereas the band edge position of penta-Sb_2C satisfies the reduction potential level only. The penta-X_2C family possess extremely high and anisotropic carrier mobility. The anisotropic characteristic can effectively reduce the recombination rate of photogenerated electron-hole pairs, resulting in higher photocatalytic efficiency. The penta-X_2C family exhibit good optical absorption in visible-ultraviolet spectrum, which is useful for improving the utilization of solar energy. Moreover, the penta-X_2C family possess relatively smaller Young's modulus and larger critical strain resulting in the great flexibility, while the auxetic penta-X_2C family has larger negative Poisson's ratio of -0.103, -0.079 and -0.077, respectively. Therefore, penta-X_2C family have potential applications not only in designing 2D electromechanical and optoelectronic devices but also in photocatalytic water splitting.

Conflicts of interest

There are no conflicts to declare.

Acknowledgments

The work was supported by the National Natural Science Foundation of China (Grants No. 11774294), the Sichuan Province Applied Science and Technology Project (Grant 2017JY0056), the R&D Program for International S&T Cooperation and Ex-

Table 3 Carrier effective masses m^*, in-plane stiffness of 2D structure C^{2D}, the deformation potential constant E_d, and the carrier mobility μ^{2D} of monolayer monolayer Penta-X$_2$C (X = P, As, Sb) along the ***a*** and ***b*** directions at room temperature.

Models	Carrier type	m_a^*/m_0	m_b^*/m_0	C_a^{2D} (N/m)	C_b^{2D} (N/m)	E_d^a (eV)	E_d^b (eV)	μ_a^{2D} $(cm^2V^{-1}s^{-1})$	μ_b^{2D} $(cm^2V^{-1}s^{-1})$
Penta-P$_2$C	electron	0.50	0.50	84.78	84.78	0.89	0.87	9.12×10^3	9.54×10^3
	hole	0.66	0.33	84.78	84.78	2.01	6.14	1.45×10^3	0.31×10^3
Penta-As$_2$C	electron	0.35	0.35	63.98	63.98	0.87	0.87	1.47×10^3	1.47×10^3
	hole	0.48	0.26	63.98	63.98	0.23	3.76	1.52×10^5	1.05×10^3
Penta-Sb$_2$C	electron	0.25	0.25	40.79	40.79	2.68	2.67	1.94×10^3	1.95×10^3
	hole	0.37	0.18	40.79	40.79	1.10	2.27	7.52×10^3	3.63×10^3

changes of Sichuan province (Grant No. 2018HH0088), and the Fundamental Research Funds for the Central Universities (2682015QM04). F. M. and J. H. acknowledge the financial support of NSF DMR 1307740 and F. M. would also like to appreciate the support from ITS summer fellowship 2018.

References

1 X. Chen, S. Shen, L. Guo and S. S. Mao, *Chem. Rev.*, 2010, **110**, 6503–6570.

2 H. Wang, L. Zhang, Z. Chen, J. Hu, S. Li, Z. Wang, J. Liu and X. Wang, *Chem. Soc. Rev.*, 2014, **43**, 5234–5244.

3 K. C. Kwon, S. Choi, J. Lee, K. Hong, W. Sohn, D. M. Andoshe, K. S. Choi, Y. Kim, S. Han, S. Y. Kim *et al.*, *J. Mater. Chem. A*, 2017, **5**, 15534–15542.

4 C.-F. Fu, X. Wu and J. Yang, *Adv. Mate.*, 2018, **0**, 1802106.

5 A. Fujishima and K. Honda, *Nature*, 1972, **238**, 37–38.

6 T. F. Jaramillo, S. Baeck, A. Kleimanshwarsctein and E. W. Mcfarland, *Macromol. Rapid Commun.*, 2004, **25**, 297–301.

7 L. Zhou, W. Wang, H. Xu, S. Sun and M. Shang, *Chem. Eur. J.*, 2009, **15**, 1776–1782.

8 Z. Cui, D. Zeng, T. Tang, J. Liu and C. Xie, *J. Hazard. Mater.*, 2010, **183**, 211–217.

9 Y. Xu, W. Zhao, R. Xu, Y. Shi and B. Zhang, *Chem. Commun.*, 2013, **49**, 9803–9805.

10 A. K. Singh, K. Mathew, H. L. Zhuang and R. G. Hennig, *J. Phys. Chem. Lett.*, 2015, **6**, 1087–1098.

11 X. Zhang, Z. Zhang, D. Wu, X. Zhang, X. Zhao and Z. Zhou, *Small Methods*, 2018, **2**, 1700359.

12 Y. Y. Lee, H. S. Jung and Y. T. Kang, *J. CO2 Util.*, 2017, **20**, 163–177.

13 T. Su, Q. Shao, Z. Qin, Z. Guo and Z. Wu, *ACS Catal.*, 2018, **8**, 2253–2276.

14 T. Hisatomi, J. Kubota and K. Domen, *Chem. Soc. Rev.*, 2014, **43**, 7520–7535.

15 B. Luo, G. Liu and L. Wang, *Nanoscale*, 2016, **8**, 6904–6920.

16 K. S. Novoselov, A. K. Geim, S. V. Morozov, D. Jiang, Y. Zhang, S. V. Dubonos, I. V. Grigorieva and A. A. Firsov, *Science*, 2004, **306**, 666–669.

17 X. Wang, K. Maeda, A. Thomas, K. Takanabe, G. Xin, J. M. Carlsson, K. Domen and M. Antonietti, *Nat. Mater.*, 2009, **8**, 76–80.

18 Z. Zhao, Y. Sun and F. Dong, *Nanoscale*, 2015, **7**, 15–37.

19 T. Yeh, J. Cihlař, C. Chang, C. Cheng and H. Teng, *Mater. Today*, 2013, **16**, 78–84.

20 U. Gupta, B. S. Naidu, U. Maitra, A. K. Singh, S. N. Shirodkar, U. V. Waghmare and C. N. R. Rao, *APL Mater.*, 2014, **2**, 092802.

21 B. Mahler, V. Hoepfner, K. Liao and G. A. Ozin, *J. Am. Chem. Soc.*, 2014, **136**, 14121–14127.

22 R. Peng, L. Liang, Z. D. Hood, A. Boulesbaa, A. A. Puretzky, A. V. Ievlev, J. Come, O. S. Ovchinnikova, H. Wang, C. Ma *et al.*, *ACS Catal.*, 2016, **6**, 6723–6729.

23 B. Sa, Y. Li, J. Qi, R. Ahuja and Z. Sun, *J. Phys. Chem. C*, 2014, **118**, 26560–26568.

24 Z. Guo, J. Zhou, L. Zhu and Z. Sun, *J. Mater. Chem. A*, 2016, **4**, 11446–11452.

25 H. L. Zhuang and R. G. Hennig, *Chem. Mater.*, 2013, **25**, 3232–3238.

26 H. L. Zhuang and R. G. Hennig, *Phys. Rev. B*, 2013, **88**, year.

27 L. A. Burton, T. J. Whittles, D. Hesp, W. M. Linhart, J. M. Skelton, B. Hou, R. F. Webster, G. Odowd, C. Reece, D. Cherns *et al.*, *J. Mater. Chem. A*, 2016, **4**, 1312–1318.

28 S. Kouser, A. Thannikoth, U. Gupta, U. V. Waghmare and C. N. R. Rao, *Small*, 2015, **11**, 4723–4730.

29 J. Liu, X. Li, D. Wang, H. Liu, P. Peng and L. Liu, *J. Mater. Chem. A*, 2014, **2**, 6755–6761.

30 X. Wang, K. Maeda, X. Chen, K. Takanabe, K. Domen, Y. Hou, X. Fu and M. Antonietti, *J. Am. Chem. Soc.*, 2009, **131**, 1680–1681.

31 Q. Zhou, Q. Chen, Y. Tong and J. Wang, *Angew. Chem.*, 2016, **55**, 11437–11441.

32 X. Zhang, X. Zhao, D. Wu, Y. Jing and Z. Zhou, *Adv. Sci.*, 2016, **3**, 1600062.

33 F. Wang, T. A. Shifa, P. He, Z. Cheng, J. Chu, Y. Liu, Z. Wang, F. Wang, Y. Wen, L. Liang *et al.*, *Nano Energy*, 2017, **40**, 673–680.

34 T. A. Shifa, F. Wang, Z. Cheng, P. He, Y. Liu, C. Jiang, Z. Wang and J. He, *Adv. Funct. Mater.*, 2018, **28**, 1800548.

35 Z. Cheng, T. A. Shifa, F. Wang, Y. Gao, P. He, K. Zhang, C. Jiang, Q. Liu and J. He, *Adv. Mate.*, 2018, **30**, 1707433.

36 Y. Ji, M. Yang, H. Dong, T. Hou, L. Wang and Y. Li, *Nanoscale*, 2017, **9**, 8608–8615.

37 S. Zhang, J. Zhou, Q. Wang, X. Chen, Y. Kawazoe and P. Jena, *Proc. Natl. Acad. Sci. U.S.A.*, 2015, **112**, 2372–2377.

38 A. Lopezbezanilla and P. B. Littlewood, *J. Phys. Chem. C*, 2015, **119**, 19469–19474.

39 Y. Xu, Z. Ning, H. Zhang, G. Ni, H. Shao, B. Peng, X. Zhang, X. He, Y. Zhu and H. Zhu, *RSC Adv.*, 2017, **7**, 45705–45713.

40 F. Shojaei, J. R. Hahn and H. S. Kang, *J. Mater. Chem. A*, 2017, **5**, 22146–22155.

41 Y. Shao, M. Shao, Y. Kawazoe, X. Shi and H. Pan, *J. Mater. Chem. A*, 2018, **6**, 10226–10232.

42 Z. Liu, H. Wang, J. Sun, R. Sun, Z. F. Wang and J. Yang, *Nanoscale*, 2018, **10**, 16169–16177.

43 M. Naseri, S. Lin, J. Jalilian, J. Gu and Z. Chen, *Front. Phys. China*, 2018, **13**, 138102.

44 M. Naseri, *Appl. Surf. Sci.*, 2017, **423**, 566–570.

45 M. M. Abutalib, *Chem. Phys. Lett.*, 2018, **708**, 188–193.

46 G. Kresse and J. Furthmuller, *Phys. Lett. B*, 1996, **54**, 11169–11186.

47 G. Kresse and D. P. Joubert, *Phys. Lett. B*, 1999, **59**, 1758–1775.

48 P. E. Blochl, *Phys. Lett. B*, 1994, **50**, 17953–17979.

49 J. P. Perdew, K. Burke and M. Ernzerhof, *Phys. Rev. Lett.*, 1996, **77**, 3865–3868.

50 H. J. Monkhorst and J. D. Pack, *Phys. Lett. B*, 1976, **13**, 5188–5193.

51 J. Heyd, G. E. Scuseria and M. Ernzerhof, *J. Chem. Phys.*, 2003, **118**, 8207–8215.

52 J. Heyd, G. E. Scuseria and M. Ernzerhof, *J. Chem. Phys.*, 2006, **124**, 219906.

53 Q. Wei and X. Peng, *Appl. Phys. Lett.*, 2014, **104**, 251915.

54 H. Wang, X. Li, P. Li and J. Yang, *Nanoscale*, 2017, **9**, 850–855.

55 C. Lee, X. Wei, J. W. Kysar and J. Hone, *Science*, 2008, **321**, 385–388.

56 R. Cooper, C. Lee, C. A. Marianetti, X. Wei, J. Hone and J. W. Kysar, *Phys. Rev. B*, 2013, **87**, 035423.

57 L. Song, L. Ci, H. Lu, P. Sorokin, C. Jin, J. Ni, A. G. Kvashnin, D. G. Kvashnin, J. Lou, B. I. Yakobson *et al.*, *Nano Lett.*, 2010, **10**, 3209–3215.

58 L. Y. Zhang, G. Qin, W. Fang, H. Cui, Q. Zheng, Q. Yan and G. Su, *Sci. Rep.*, 2016, **6**, 19830–19830.

59 A. J. Mannix, X. Zhou, B. Kiraly, J. D. Wood, D. Alducin, B. D. Myers, X. Liu, B. L. Fisher, U. Santiago, J. R. Guest *et al.*, *Science*, 2015, **350**, 1513–1516.

60 J. Jiang and H. S. Park, *Nat. Commun.*, 2014, **5**, 4727.

61 M. Yagmurcukardes, H. Sahin, J. Kang, E. Torun, F. M. Peeters and R. T. Senger, *J. Appl. Phys.*, 2015, **118**, 104303.

62 R. Abe, *J. Photoch. Photobio. C*, 2010, **11**, 179–209.

63 T. Korn, S. Heydrich, M. Hirmer, J. Schmutzler and C. Schüller, *Appl. Phys. Lett.*, 2011, **99**, 102109.

64 S. Saha, T. P. Sinha and A. Mookerjee, *Phys. Rev. B*, 2000, **62**, 8828–8834.

65 M. Qiao, Y. Chen, Y. Wang and Y. Li, *J. Mater. Chem. A*, 2018, **6**, 4119–4125.

66 G. Schusteritsch, M. Uhrin and C. J. Pickard, *Nano Lett.*, 2016, **16**, 2975–2980.

67 J. Qiao, X. Kong, Z. Hu, F. Yang and W. Ji, *Nat. Commun.*, 2014, **5**, 4475–4475.

68 S. Sun, F. Meng, H. Wang, H. Wang and Y. Ni, *J. Mater. Chem.*, 2018, **6**, 11890–11897.

69 Y. Song, J. Yuan, L. Li, M. Xu, J. Wang, K. Xue and X. Miao, *Nanoscale*, 2019.

70 J. Bardeen and W. Shockley, *Phys. Rev.*, 1950, **80**, 72–80.

71 J. Chen, J. Xi, D. Wang and Z. Shuai, *J Phys. Chem. Lett.*, 2013, **4**, 1443–1448.

72 M. Long, L. Tang, D. Wang, Y. Li and Z. Shuai, *ACS Nano*, 2011, **5**, 2593–2600.

73 Y. Guo, Q. Wu, Y. Li, N. Lu, K. Mao, Y. Bai, J. Zhao, J. Wang and X. C. Zeng, *Nanoscale Horiz.*, 2019, **4**, 223–230.

74 Y. Cai, G. Zhang and Y.-W. Zhang, *J. Am. Chem. Soc.*, 2014, **136**, 6269–6275.

75 S. Bruzzone and G. Fiori, *Appl. Phys. Lett.*, 2011, **99**, 222108.

76 C. Long, Y. Liang, H. Jin, B. Huang and Y. Dai, *ACS Appl. Energy Mater.*, 2019, **2**, 513–520.

77 R. Meng, X. Sun, D. Yang, J. Bao and X. Chen, *Appl. Mater. Today*, 2018, **13**, 276–284.

78 Y. Jing, Y. Ma, Y. Wang, Y. Li and T. Heine, *Chem.-Eur. J.*, 2017, **23**, 13612–13616.

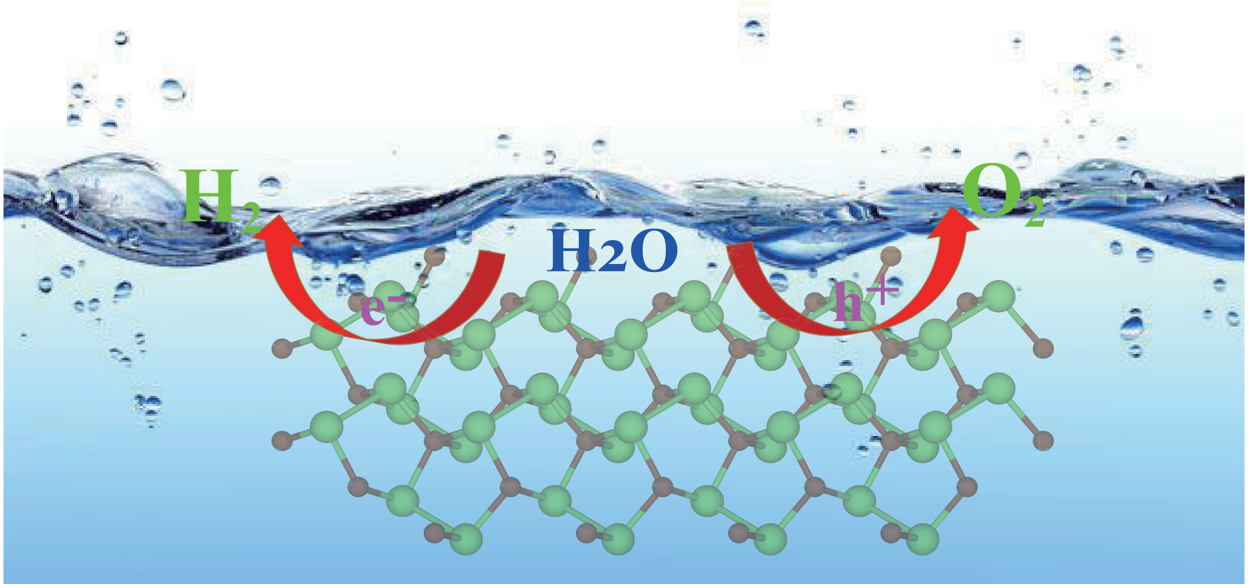

Penta-X_2C (X = P, As and Sb): A novel two dimensional family for photocatalytic water splitting.